Title	Damage detection in bridges based on patterns of dynamic amplification
Authors(s)	González, Arturo, Mohammed, Omar
Publication date	2019-07
Publication information	González, Arturo, and Omar Mohammed. “Damage Detection in Bridges Based on Patterns of Dynamic Amplification.” John Wiley & Sons Ltd., July 2019. https://doi.org/10.1002/stc.2361.
Publisher	John Wiley & Sons Ltd.
Item record/more information	http://hdl.handle.net/10197/10162
Publisher's statement	This is the peer reviewed version of the following article: González, A, Mohammed, O. Damage detection in bridges based on patterns of dynamic amplification. Structural Control Health Monitoring.26(7). Article number: e2361. https://doi.org/10.1002/stc.2361, which has been published in final form at http://onlinelibrary.wiley.com/doi/10.1002/stc.2361. This article may be used for non-commercial purposes in accordance with Wiley Terms and Conditions for Self-Archiving.
Publisher's version (DOI)	10.1002/stc.2361

Damage Detection in Bridges based on Patterns of Dynamic Amplification

Arturo González [1, 3], Omar Mohammed [2, 3 *]
[1] Associate Professor, email: arturo.gonzalez@ucd.ie
[2] Researcher, email: omar.sattar@ucdconnect.ie
[3] School of Civil Engineering, University College Dublin, Ireland
[*] Corresponding author. Postal address: School of Civil Engineering, University College Dublin, Newstead, Belfield, Dublin 4, Ireland.
Phone number: +353 1 7163229.
Email address: omar.sattar@ucdconnect.ie, omaralanni1984@gmail.com

Abstract

The pattern of Dynamic Amplification Factor (DAF) of the bridge strain response to a moving vehicle versus vehicle velocity is used to develop a level I damage technique. The challenge is to detect damage that causes only a small and difficult to detect frequency change with respect to the healthy condition. For this purpose, a damage index is defined based on subtracting the DAF-velocity pattern for the bridge in a prior healthy state from the DAF-velocity pattern corresponding to the damaged bridge. Simulations from a 3D vehicle-bridge interaction model are employed to show how the index increases with damage. The influence of the location of the strain sensors, the location and severity of the damage, the road roughness, the corruption of measurements by noise, and the velocity range on the robustness of the technique are analysed. The relative changes in the proposed index as a result of damage are shown to clearly outperform the associated relative changes in frequencies, even for measurement locations far apart from the damage.

Keywords: damage identification; vehicle bridge interaction; dynamic amplification factor; bridge dynamics; structural health monitoring

1. Introduction

There is an ongoing effort in devising strategies that make the best use of the available resources for early damage detection in bridges. Wong and Yao [1] demonstrate that Structural Health Monitoring (SHM) can be exploited as a segment of the risk management process for a bridge, where SHM can abet in indicating any sort of structural failure. SHM makes sure that relevant information is provided to the owners of the structure to allow them taking action on time for effective repair [2]. Popular SHM techniques are based on measuring vibrational characteristics of the structure (i.e., mode shapes, frequencies, and damping) on a continuous basis. Döhler et al [3] quantify the uncertainty surrounding the estimation of natural frequencies and damping ratios due to noise, finite data length, non-stationary excitations, model order reduction or other operational influences associated with the first five mode shapes of the S101 prestressed concrete bridge in Austria via stochastic subspace identification methods. Coefficients of variation in the estimation of the first natural frequency of 0.12 and of 0.29 are found for healthy (4.036 Hz) and damaged (4.017 Hz) versions respectively with no relevant temperature or other environmental changes. The level of this uncertainty will vary with the nature of the excitation forces (i.e., traffic loading), environmental variables (i.e., temperature and temperature gradients, humidity, wind speed and others) and damage or deterioration due to ageing. In particular, changes in frequencies as a result of seasonal/temperature variations can easily hinder the effect of damage. Liu et al [4] review the literature on measured frequencies with temperature, noting a daily change of 4.7%, 6.6%, and 5.0%, for the first three modal frequencies of a bridge deck in New Mexico that varied temperature by about 22°C, and changes of 14%-18% for the first four modal frequencies of the Z24 bridge in Switzerland during 10 months. For a reinforced concrete beam-and-slab, [4] suggest that modal frequencies will decrease 0.12%-0.33% per degree Celsius with respect to the modal frequencies at 0°C, being the variation of concrete elasticity modulus with temperature the main cause of these changes. There are two approaches towards separating effects due to operational conditions from effects due to damage: (i) input-output methods, where operational variables such as temperature, humidity and/or traffic loading are measured together with modal properties to establish their relationship, i.e., via the polynomial chaos expansion method proposed by Spiridonakos et al [5], and (ii) output-only methods, where operational variables are treated as embedded variables that do not need to be measured, as their influence will be discarded via methods such as neural networks, factor analysis [6], Principal Component Analysis (PCA) [7,8] or Kernel PCA [9].

Rytter [10] classifies vibration-based damage identification approaches into four levels of increasing degree of complexity that establish: Whether damage occurred or not (level I), the position of damage (level II), its quantification (level III) and the remaining lifespan of the structure (level IV). Fan and Qiao [11] carry out a thorough review of the available vibration-based damage detection methods. While there is a group of model-based SHM methods that can reach level IV depending on the amount of available data and the complexity of the finite element model to be updated, they are time-consuming compared with data-driven SHM methods, which are typically level I or II and able to provide results in real-time. There is a third group of methods that combines model-based and data-driven SHM, i.e., the damage locating vector and statistical fault isolation methods, as discussed by Limongelli et al [12], who compare data-driven with model-based SHM using the measurements of the post-tensioned concrete two-cell box Z24 bridge girder.

Cebon [13] argues that heavy vehicles induce vibrations in the bridge that can cause damage to the structure and consequently, they affect its lifespan and safety. A pavement-based Weigh-In-Motion (WIM) system placed prior to the bridge (i.e., bending plate or piezoelectric sensors embedded in the pavement) can be employed to identify and prevent overloading. Load monitoring is the basis for the level I damage detection technique proposed by Cantero and González [14] that measures truck loads via two means: (1) a pavement-based WIM system, and (2) a Bridge Weigh-In-Motion (B-WIM) system (i.e., from strains measured on the bridge soffit based on the concept of influence lines). The principle of their technique is that the estimation of truck loads by both WIM and B-WIM systems should be correlated, except for environmental changes or deterioration. Bridge strains are commonly used as input to the B-WIM algorithm given that they are often reliable and offer high-resolution levels. However, the technique proposed by [14] can be costly, as inputs from both pavement-based and bridge-based WIM installations are needed. In the approach by [14], if the bridge gets damaged and becomes more flexible, truck loads will be overestimated by the B-WIM system (i.e., values derived using an original healthier influence line of smaller magnitude) when compared with the WIM system. Therefore, damage in the form of stiffness loss localised in a narrow portion of the bridge will go unnoticed to the static component of strain in a statically determinate structure, unless the transducer is positioned near the damaged portion.

This paper intends to overcome some of the limitations in [14] using the concept of Dynamic Amplification Factor (DAF) for damage detection purposes. Even though the static component of strain may overlook damage, a localised stiffness loss will generally affect the dynamic component of strain and measured strain (static plus dynamic) caused by the forces of a moving heavy vehicle. The impact of damage on the measured strain will depend on the location and size of damage, the vehicle velocity and configuration, and the dynamic characteristics of the vehicle-bridge-road interaction system. Brady et al [15] define DAF as the maximum total load effect (static plus dynamic) divided by the maximum static load effect at a specific bridge location due to a given vehicle travelling on a fixed path at a uniform velocity. When DAF is calculated for a range of vehicle velocities, there appears to be a pattern defined by a series of DAF peaks and throughs that tend to increase with higher velocities [16-25]. Brady et al [15] and González et al [20] provide a deep insight into why peaks of DAF develop at some critical velocities. Generally speaking, the static component of strain will increase as the load moves towards the measurement location, i.e., it is directly related to the vehicle velocity and to the distance to the sensor. In general, the dynamic component oscillates between maxima and minima, where one cycle is related to a natural period of vibration of the bridge. On the one hand, low DAFs will be the outcome of destructive interference between static and dynamic components of the bridge response (i.e., the maximum static coinciding with a minimum value of the dynamic oscillations). On the other hand, high DAFs will be motivated by the simultaneous occurrence of high values of both static and dynamic components of the response. The shape and magnitude of the DAF against velocity pattern are exploited in this paper to propose a new level I damage detection technique.

Given that DAF is a ratio of strains, the requirements for calibration of sensors are not as strict as for other methods where exact strains may be needed. It requires that a DAF-velocity pattern is gathered for the structure in a healthy state to be used as a reference basis for detecting damage in the future. It builds on a preliminary investigation by the authors [25] using a simply supported 1D Finite Element (FE) beam and a planar vehicle. Here, the bridge is modelled as a simply supported 2D FE plate and the vehicle as a 3D sprung mass model to test the feasibility of using variations in DAF patterns as a monitoring tool in a more realistic situation. First, the characteristics of the models used in the simulations are defined. Then, contour plots of measured DAF against velocity are calculated at several bridge locations to describe and comprehend the fundamental pattern, and how it changes for different stages of stiffness loss. Finally, the impact of the vehicle and its velocity, the unevenness of the road profile and the noise due to corrupted strain measurements on the accuracy of the technique are subjects of investigation.

2. Simulation of the response of a bridge to a moving vehicle

There is an extensive literature about how to model the dynamic interaction between a vehicle and a bridge using FE models [26-28]. In the case of highway bridges and typical trucks, uncoupled and coupled approaches are equivalent in most cases, and an uncoupled Vehicle-Bridge Interaction (VBI) model is usually preferred for computational efficiency. In the coupled VBI, there is a unique system matrix with time-dependent properties that change as the vehicle moves. In the uncoupled VBI, the equations of motion of the vehicle and the bridge are treated as two separate subsystems to obtain a solution independently. The matrixes of the two subsystems remain constant throughout the duration of the simulation and they have a smaller dimension than the unique system matrix of the coupled approach. Modal superposition method can be used to solve the equations of motion of the bridge sub-system, which reduces the computation effort considerably. Modal superposition transforms the original matrixes with non-zero off-diagonal terms into a smaller set of independent modal coordinate equations (i.e., zero off-diagonal terms). The total dynamic response is then obtained by superposition of the response obtained for each modal coordinate.

2.1 Finite element modelling of vehicle-bridge interaction

One of the major causes of excitation in vehicle-induced bridge vibrations is the roughness of the road [16,29-33]. As per ISO 8608 [34], a stochastic road carpet is generated in terms of the function of power spectral density of vertical displacements accompanied by the inverse fast Fourier transform technique illustrated by Cebon and Newland [35]. A random phase angle $\emptyset_i$ along with a uniform probabilistic distribution in the 0-2π range is used for each spatial wave. The height of the road irregularities is correlated in the transverse direction. A Moving Average Filter (MAF) is applied to the generated road profile heights over a distance of 0.24 m to simulate the attenuation of short wavelength disturbances by the tyre contact patch [36,37].

An uncoupled VBI algorithm built in Matlab [38] is employed for calculating the response of a bridge plate model to the crossing of the 3D 5-axle truck over a road profile at a uniform velocity. The iterative procedure implemented in this paper follows Cantero et al [21]. Initially, vehicle forces are estimated using the equation of motion of the vehicle (Equation (1)).

$$M_v\ddot{w}_v + C_v\dot{w}_v + K_v w_v = f_v \tag{1}$$

where M_v, C_v, and K_v are mass, damping and stiffness matrices of the vehicle respectively, and $\ddot{w}_v$, $\dot{w}_v$ and w_v are the vectors corresponding to nodal accelerations, nodal velocities and nodal displacements. f_v is a vector containing the time-varying forces imposed on the vehicle's DOFs. The system of equations defined by Equation (1) is attained from applying equilibrium of forces and moments at all Degrees of Freedom (DOFs) as explained by Cantero et al [39]. f_v is a vector containing the time-varying forces imposed on the vehicle's DOFs, which is a combination of tyre properties (stiffness/damping) and height of the road profile and bridge displacements. At this point, there is not an estimation of bridge displacements yet, therefore, a preliminary time history of vehicle forces is derived with Equation (1) using the road profile only (i.e., ignoring the deflected shape of the bridge). These forces must be applied to the bridge for a first estimation of bridge displacements via the general equation of motion of the bridge model given by Equation (2).

$$M_b\ddot{w}_b + C_b\dot{w}_b + K_b w_b = f_b \tag{2}$$

where M_b, C_b and K_b are mass, damping and stiffness matrices respectively of the bridge model, $\ddot{w}_b$, $\dot{w}_b$ and w_b are vectors of time-varying nodal bridge acceleration, velocity and displacement respectively and, f_b are time-varying forces at the nodal DOFs of the bridge model. The forces f_v obtained from Equation (1) cannot be directly applied to Equation (2). They need to be converted first to equivalent forces f_b acting on the nodes of the bridge FE directly underneath. Equation (3) is used for this purpose.

$$f_b = L \times f_v \tag{3}$$

where f_b is a matrix p x 1, f_v is a vector p_f x 1, and L is a $p \times p_f$ location matrix that relates the p_f wheel forces to equivalent forces acting on the p DOFs of the bridge. For instance, column 1 of location matrix L distributes the first wheel force to the DOFs of the specific bridge FE where the force is applied, the second column of L distributes the second wheel force to the corresponding bridge DOFs, the third column distributes the third wheel force to the bridge DOFs, and so on. In the case of a bridge model made of plate elements with 4 DOFs at each node, the time-varying location matrix L will adopt a form such as in Equation (4).

$$L=\begin{bmatrix} 0 & 0 & \cdots & 0 & \cdots & 0 \\ . & . & \cdots & . & \cdots & . \\ N_1(x_1,y_1) & . & \cdots & . & \cdots & . \\ N_2(x_1,y_1) & N_1(x_2,y_2) & \cdots & . & \cdots & . \\ . & N_2(x_2,y_2) & \cdots & N_1(x_i,y_i) & \cdots & . \\ N_{16}(x_1,y_1) & . & \cdots & N_2(x_i,y_i) & \cdots & N_1(x_{10},y_{10}) \\ . & N_{16}(x_2,y_2) & \cdots & . & \cdots & N_2(x_{10},y_{10}) \\ . & . & \cdots & N_{16}(x_i,y_i) & \cdots & . \\ . & . & \cdots & . & \cdots & N_{16}(x_{10},y_{10}) \\ . & . & \cdots & . & \cdots & . \\ 0 & 0 & \cdots & 0 & 0 & 0 \end{bmatrix} \tag{4}$$

where $N_1(x_i,y_i)$ to $N_{16}(x_i,y_i)$ are the shape functions corresponding to the 16 DOFs of the plate element, and x_i and y_i are the longitudinal and transverse distances between a node of the plate element and the wheel force i, which will vary with time.

An iterative procedure is needed to ensure compatibility of displacements between the DOFs shared by the vehicle and by the bridge. In a 1st iteration, the bridge displacements w_b obtained above (i.e., $w_{b,0}$) are added to the road profile (i.e., r) to recalculate the vehicle forces f_v using Equation (1) (i.e., $f_{v,1}$). The new vehicle forces $f_{v,1}$ are used to obtain a new f_b via Equation (3) (i.e., $f_{b,1}$). The forces $f_{b,1}$ are then applied to Equation (2) to obtain the bridge displacements w_b corresponding to iteration 1 (i.e., $w_{b,1}$). At the end of the 1st iteration, the differences between the initial deflected shape ($w_{b,0}$) and the deflected shape resulting from the 1st iteration ($w_{b,1}$) are calculated. Based on the convergence criterion proposed by Green and Cebon [40], it is established that if this variation is more than 2% of the highest bridge deflection, then a 2nd iteration, where the bridge displacements $w_{b,1}$ obtained in the 1st iteration are added to the road profile to calculate the new vehicle forces $f_{v,2}$, $f_{b,2}$, and the new displacements $w_{b,2}$, is needed. Iterations will have to be repeated until the differences between two consecutive iterations (i.e., $w_{b,i}$ and $w_{b,i+1}$) fulfil the criterion.

2.2 Bridge, vehicle and road scenarios

Equations (1) and (2) are solved via application of the Newmark-Beta direct integration method with a time increment of 0.001 s and integration constants values of Delta = 0.5 and Beta = 0.25. The overall length, width, and depth of the bridge model are 20 m, 9 m, and 1 m respectively. The bridge is modelled as an FE orthotropic thin plate discretized into rectangular $C1$ plate elements with four nodes [41]. In comparison to the standard Kirchhoff's plate element [42], this element has one additional DOF per node, i.e., twist, to avoid the discontinuity of slope alongside the edge elements. Hence, this element has a total of 16 DOFs and 4 DOFs per node: vertical displacement, one twist and two rotations (X - longitudinal- and Y -transverse- directions). The dimensions of the discretised plate elements are 0.5 m × 0.5 m. Therefore, the bridge model has a total of 3078 DOFs. The shape functions associated with the vertical displacement, the rotations about the X- and Y- directions and the twist of one node of the plate element that will be used to populate the location matrix (Equation (4)), are given by Equations (5), (6), (7) and (8) respectively [17].

$$N_1(x_i,y_i)=(b+2y_i)(b-y_i)^2(a+2x_i)(-x_i+a)\frac{1}{a^3b^3} \tag{5}$$

$$N_2(x_i, y_i) = -y_i(b-y_i)^2(a+2x_i)(-x_i+a)^2\frac{1}{a^3b^2} \tag{6}$$

$$\begin{aligned} N_3(x_i, y_i) = {} & x_i(b-y_i)(-2x_iab^3 + x_i{}^2b^3 + a^2b^2 - 2x_iy_iab^2 + x_i{}^2y_ib^2 \\ & + y_ia^2b^2 - 14x_iy_i{}^2ab + 10x_i{}^2y_i{}^2b - 2y_i{}^2a^2b + 18x_iy_i{}^2a^2 - 12x_i{}^2y_i{}^2a)\frac{1}{a^2b^4} \end{aligned} \tag{7}$$

$$\begin{aligned} N_4(x_i, y_i) = {} & x_iy_i(b-y)(-2x_iab^2 + x_i{}^2b^2 + a^2b^2 - 7x_iy_iab \\ & + 5x_i{}^2y_ib - y_ia^2b + 9x_iy_ia^2 - 6x_i{}^2y_ia)\frac{1}{a^2b^3} \end{aligned} \tag{8}$$

where a and b are the dimensions of the plate element, i.e., 0.5 m.

Typical bridge properties are selected based on [43,44]. The moduli of elasticity in longitudinal and transverse directions are 35 GPa and 32.2 GPa respectively, and the shear modulus is 14 GPa. Poisson's ratios in longitudinal and transverse directions are assumed to be 0.2. Damping is modelled using the Rayleigh approach (Equation (9)) with the constants α and β being 1.222554 and 0.000532 respectively to yield a damping ratio ζ of 0.03 for the first two modes.

$$C_\mathrm{b} = \alpha M_b + \beta K_b \tag{9}$$

Figure 1 shows the 5-axle tractor-semitrailer model, which is composed of two main sub-structures, tractor and semitrailer, depicted as grouped masses. This truck model has 15 DOFs in the form of wheel hop displacements (y_{ui} at every un-sprung wheel's mass m_{ui} with i = 1 to 10), tractor bounce displacement, y_T, tractor pitch rotation, θ_T, tractor rolling rotation, β_T, semi-trailer pitch rotation, θ_s, and semi-trailer rolling rotation, β_s. This model assumes a negligible lateral and yaw movement.

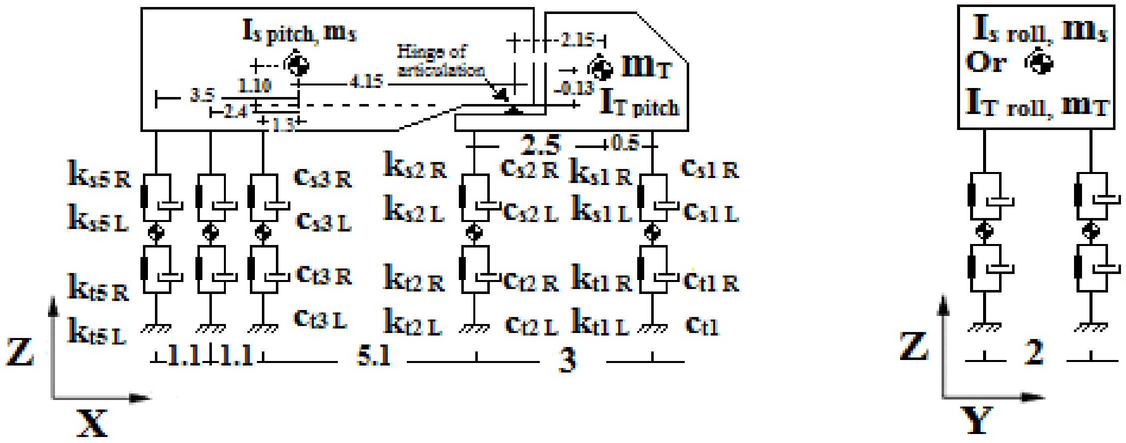

(a) (b)

Figure 1. General vehicle model sketch: (a) side view and (b) back view (all dimensions in meters).

Table 1 gives the mechanical properties of the vehicle based on [21]. The static wheel weights are 24.94 kN, 54.39 kN, 39 kN, 39.02 kN and 39.02 kN for vehicle axles 1 to 5 respectively based on the distribution of gross vehicle weight proposed by [20]. The body masses have a bouncing frequency of 1.49 Hz for the tractor, pitching frequencies of 2.30 Hz for the tractor and 1.49 Hz for the semitrailer, and rolling frequencies of 3.01 Hz for the tractor and 1.59 Hz for the semitrailer. Axle hop frequencies of 8.96 Hz, 10.7 Hz, and 11.6 Hz are found for the 1st axle, 2nd axle, and axles within the rear tridem respectively.

Table 1. Properties of the 5-axle truck model (R and L refer to Right and left wheel respectively)

Symbol	Property	Value	Units
m_T	Tractor body mass	4500	kg
m_s	Semi-trailer body mass	31450	kg
m_{u1}	Tractor front axle	700	kg
m_{u2}	Tractor rear axle	1000	kg
m_{u3} to m_{u5}	The mass for each axle of the Semitrailer	1100	kg
$I_{T\,pitch}$	Tractor pitch moment of inertia (about Y-axis)	4875	kg m^2
$I_{T\,roll}$	Tractor rolling moment of inertia (about X-axis)	3000	kg m^2
$I_{s\,pitch}$	Semi-trailer pitch moment of inertia (about Y-axis)	123000	kg m^2
$I_{s\,roll}$	Semi-trailer rolling moment of inertia (about X-axis)	21000	kg m^2
Ks_{1R}, Ks_{1L}	Suspension stiffness of tractor front axle	200×10^3	N m^{-1}
Ks_{2R}, Ks_{2L}	Suspension stiffness of tractor rear axle	500×10^3	N m^{-1}
$Ks_{3\text{-}5R}$, $Ks_{3\text{-}5L}$	Suspension stiffness of each of the semitrailer axles	500×10^3	N m^{-1}
$Cs_{1\text{-}5R}$, $Cs_{1\text{-}5L}$	Axles suspension damping	5×10^3	Ns m^{-1}
K_{t1R}, K_{t1L}	Tyre stiffness of tractor front axle	875×10^3	N m^{-1}
K_{t2R}, K_{t2L}	Tyre stiffness of tractor rear axle	1750×10^3	N m^{-1}
$K_{t3\text{-}5R}$, $K_{t3\text{-}5L}$	Tyre stiffness of each of the semitrailer axles	1750×10^3	N m^{-1}
$C_{t1\text{-}5R}$, $C_{t1\text{-}5L}$	Axles tyre viscous damping	3×10^3	Ns m^{-1}

This paper considers two road classes: class ‘A’ (very good) with a geometric spatial mean of 16×10^{-6} m^3/cycle and class ‘B’ (good) with a geometrical spatial mean of 64×10^{-6} m^3/cycle. Figure 2 illustrates the carpets with very good and good road classes generated for the bridge. In addition to the bridge carpets shown in these figures, an approach road of 100 m length has been added before the bridge to excite the vehicle initially before moving onto the bridge.

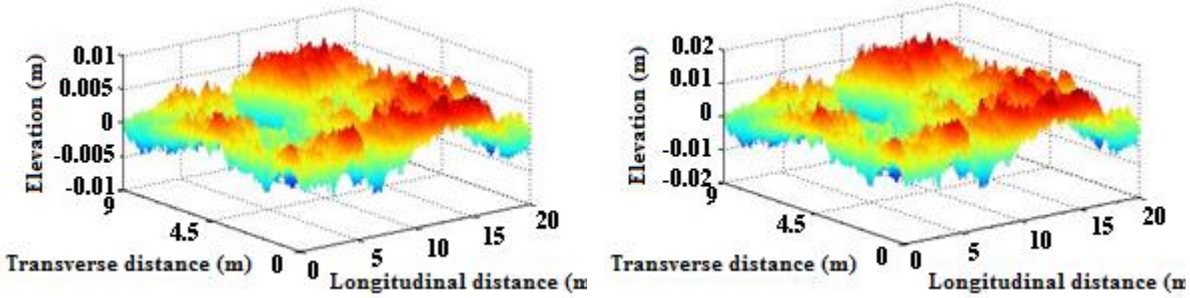

(a) (b)

Figure 2. Road carpets generated for the bridge: (a) class ‘A’ and (b) class ‘B’.

Damage has been simulated in three different regions of the bridge: Full-through damage that covers the full bridge width (i.e., 9 m), part-through damage 1 that covers the half of the bridge width (i.e., 4.5 m) where the vehicle is travelling and part-through damage 2, which covers the half of the bridge width (i.e., 4.5 m) where the vehicle is not travelling. The damage is assumed to be due to a crack at the bottom of the section, and following Sinha et al [45], it is modelled as a stiffness reduction governed by a triangular variation. I.e., the crack produces a loss in stiffness in the bridge over an area of three times the bridge depth (= 1 m in the bridge model under investigation), i.e., the total damage extends longitudinally over a strip of 3 m. The three damaged regions are modelled with two severities: (i) varying linearly from 30% stiffness loss in the central elements of the affected area to a healthy condition at 1.5 m distance, (ii) varying linearly from 10% stiffness loss in the central elements of the affected area to a healthy condition at 1.5 m distance. It must be noted that stiffness losses of 30% and 10% correspond to crack sizes of 11.21 cm (crack to slab depth ratio of 0.1121) and 3.45 cm (crack to slab depth ratio of 0.0345) respectively. A well-known level I damage detection technique consists of monitoring and correlating changes in frequencies with temperature. Table 2 provides percentage of changes in the first natural frequency of the damaged scenarios with respect to the healthy one for reference purposes. It can be seen that the change in frequency is –0.70% for the 10% part-through stiffness loss, which would be difficult to identify early for a level I damage detection technique based only on frequency changes due to the influence of noise and environmental effects. Out of the six scenarios being considered, –5.23% is the most significant relative change in frequency taking place for 30% full-through stiffness loss.

Table 2. Main frequencies of the seven bridge conditions

Bridge type	Stiffness loss	First natural frequency (Hz)	Relative change in natural frequency (%)
Healthy bridge	0	4.24	0
Full-through damage	10 %	4.18	–1.41
Part-through damage 1		4.21	–0.70
Part-through damage 2		4.21	–0.70
Full-through damage	30 %	4.018	–5.23
Part-through damage 1		4.14	–2.35
Part-through damage 2		4.14	–2.35

Figure 3 shows a plan view of the bridge model together with the size and location of the region affected by damage coloured in black. This figure also includes a sketch of the vehicle wheel paths. The direction followed by the vehicle is from left to right in all simulations. The positions of the simulated strain sensors (A1-A5 at ¼ span), (B1-B5 at ½ span) and (C1-C5 at ¾ span) are also represented. Sensors are located in three different sections set apart longitudinally by 5 m. For the same longitudinal section, the transverse distance between consecutive sensor locations is 1.5 m, i.e., from A1 to A2, from B1 to B2 or from C1 to C2.

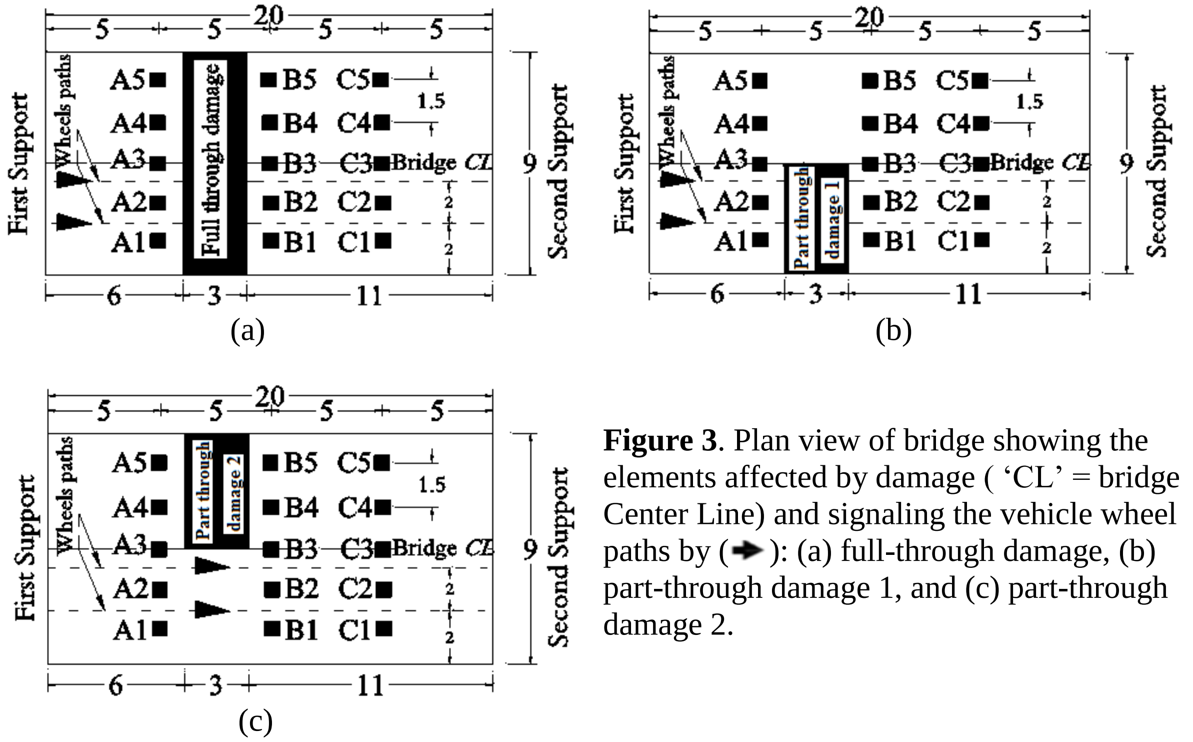

(a)

(b)

(c)

Figure 3. Plan view of bridge showing the elements affected by damage ('CL' = bridge Center Line) and signaling the vehicle wheel paths by (➡): (a) full-through damage, (b) part-through damage 1, and (c) part-through damage 2.

3. Calculation of dynamic amplification factor

Prior research has employed DAF to quantify the dynamic amplification of bridge response with respect to the static component as a result of moving vehicles, and to calibrate traffic load models for bridges. In this paper, the objective behind the use of DAF is to detect damage in a bridge monitored with 15 sensors measuring longitudinal (X-direction) strain placed at equal distances (Figure 3). DAF is obtained using VBI simulations (Section 2.4) for every sensor, i.e., the ratio of maximum total (static plus dynamic) strain to maximum static strain due to a specific vehicle. In the strain calculations, the neutral axis is assumed to be positioned at 0.5 m from the measurement point. In a real-life situation, the total strain will be measured, but the static component of the strain can only be approximated. Therefore, the static response is inferred by applying a MAF to the total response, as recommended by [46]. The Fast Fourier Transform in Figure 4 illustrates how the influence of bridge dynamics is minimised through filtering for a variety of velocities. The first natural frequency of the bridge, i.e., 4.24 Hz, is identified by an evident bump in Figure 4(a). If the MAF is applied to the total response using a filter span equal to the period of the aforementioned frequency, then, the 1st natural frequency of the bridge is eliminated from the spectra (Figure 4(b)).

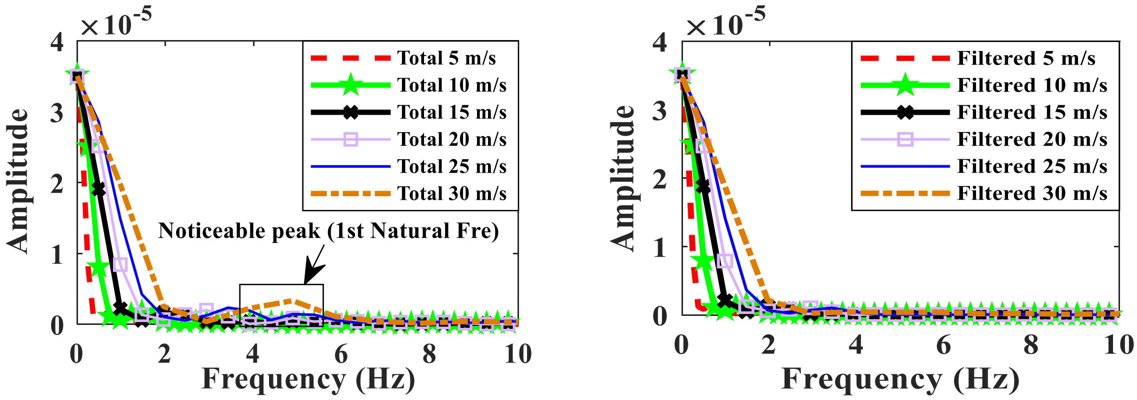

(a) (b)

Figure 4. Frequency domain of the bridge total response at sensor B3 when the vehicle is travelling at different velocities: (a) Before applying MAF and (b) After applying MAF.

The original strain signal is made up of a number of discretized strain values for each point in time that depends on the scanning frequency, the vehicle configuration and velocity, and the bridge length. For the MAF to work efficiently, the number of consecutive strain measurements to be averaged needs to relate to the natural period of the bridge. The MAF for a strain value at given point in time is calculated taking that point as the centre of the filter span and an equal number of points on either side. For example, if the number of simulated measurements per second is p, and the first natural period of the structure is T_1 (= 1/4.24 seconds in this case), the result of applying the MAF at a specific point in time is established by adding together the value of the point before filtering, and the values of $(p\cdot T_1-1)/2$ points before filtering to the left and to the right of the point, and dividing the sum of all values by $p\cdot T_1$. Additional fictional points are mirrored at both signal ends by antisymmetric padding to adjust the length of the filter at the initial and final points. This mirroring facilitates that, after applying the MAF, a zero value is assigned to the first measurement point, i.e., when the first axle is located on the 1st support. Figure 5 shows the effect of applying a MAF to the longitudinal strain response due to the vehicle crossing at 20 m/s.

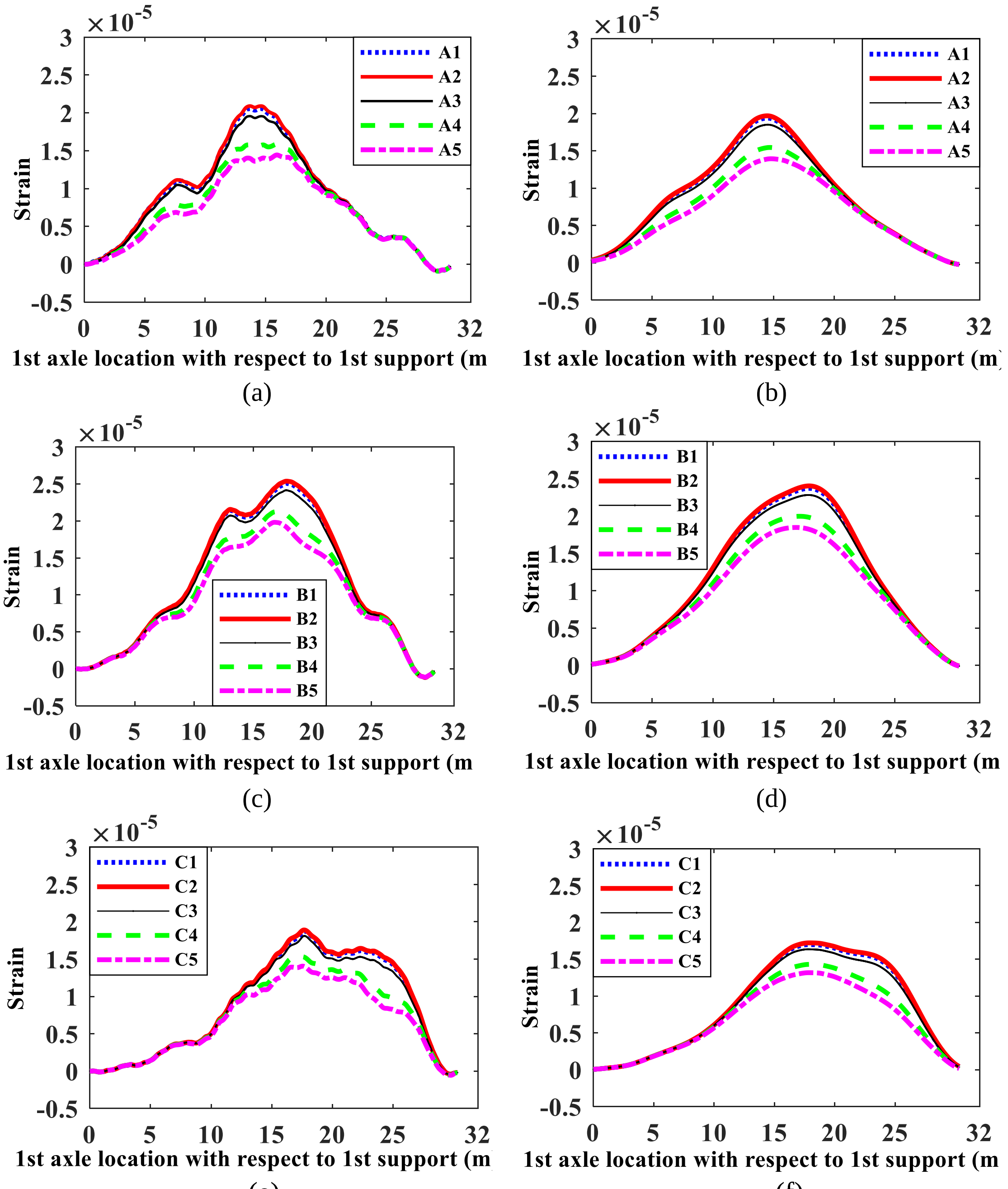

(a) (b)

(c) (d)

(e) (f)

Figure 5. Total and filtered strains versus position of 1st axle when the vehicle crosses the bridge at 20 m/s: (a) Total response at A sensors (1/4 span), (b) Filtered response after MAF at A sensors (1/4 span), (c) Total response at B sensors (1/2 span), (d) Filtered response after MAF at B sensors (1/2 span), (e) Total response at C sensors (3/4 span), and (f) Filtered response after MAF at C sensors (3/4 span).

Although the number of points defining the filter span does not depend on the velocity, the higher the velocity, the lower the number of available measurements on the bridge becomes. If there are fewer measurement points, then there will be less, and possibly incomplete, cycles of the dynamic component oscillating around the static component. Additionally, the static component has a more significant content of high frequencies at higher velocities. Obviously, the filtered strain may differ from the exact static strain when the MAF removes the highest frequency content of the static component. The latter is more likely to occur for higher velocities. The theoretical exact strain will depend on the stiffness matrix of the bridge, K_b, and the values and positioning of the static wheel weights on the bridge (i.e., using Equation (2) with $\ddot{w_b} = 0$ and $\dot{w}_b = 0$). Figure 6 compares the exact and filtered static responses for three velocities. It is evident that part of the static content is inadvertently removed as a result of using the first natural period of the bridge to establish the duration of the filter span of the MAF. In this case, the maximum static strain and DAF will be underestimated and overestimated respectively. However, even if the filtering magnifies DAF values to some extent, the following sections demonstrate that estimated DAF-velocity patterns can still be successfully referred to an estimated baseline DAF-velocity pattern obtained in healthy conditions for damage detection purposes.

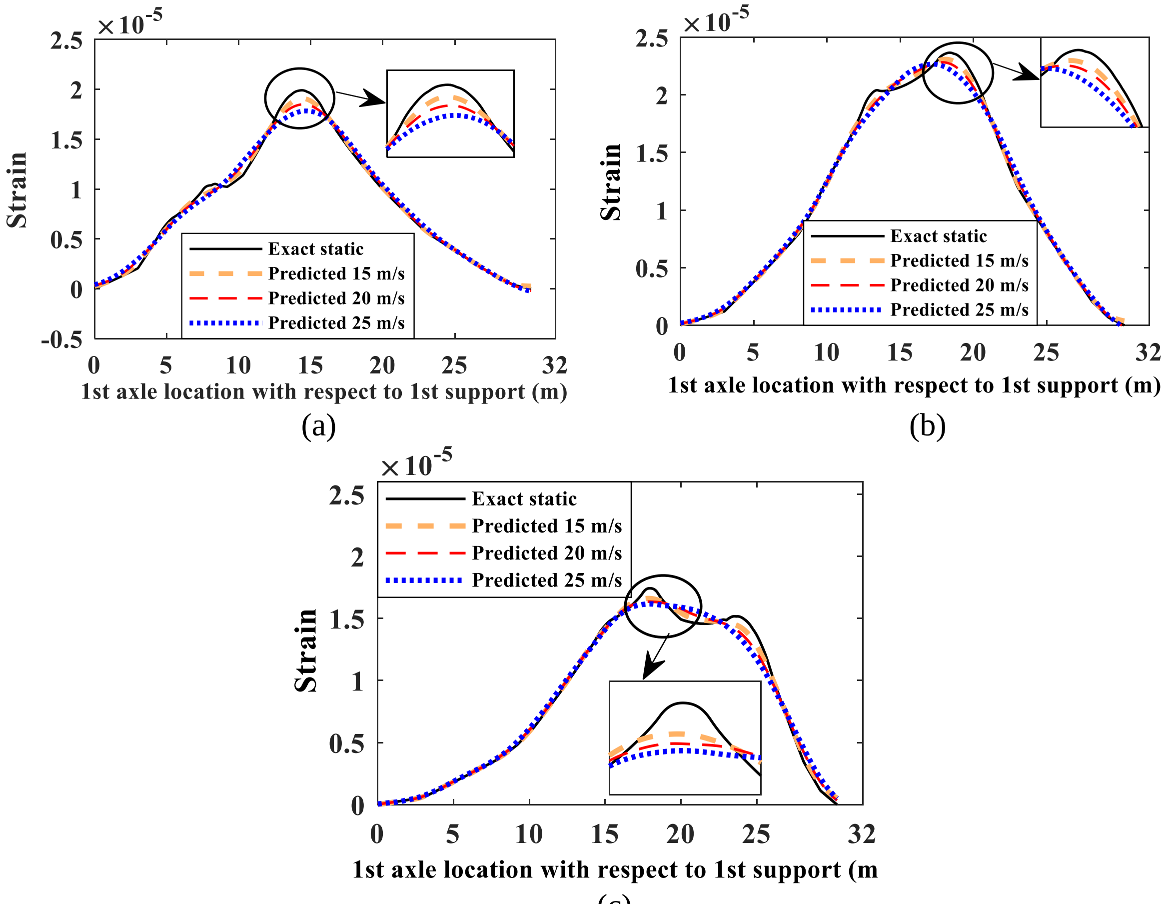

(a) (b)

(c)

Figure 6. Comparison of exact and predicted (filtered) responses at 15, 20 and 25 m/s for three sensor locations: (a) sensor A3 (1/4 span), (b) sensor B3 (1/2 span), and (c) sensor C3 (3/4 span).

4. Relative changes in DAF for damage detection purposes

The damage detection algorithm relies on available information about the pattern of DAF versus velocity for a healthy bridge to compare with, for the same vehicle or vehicle fleet and the same velocity interval. Hence, the DAF-velocity pattern is obtained first for the response of the bridge in a healthy condition (Section 4.1) to the vehicle defined in Section 2. DAF is approximated here by the ratio of total to filtered response and calculated for velocities from 10 km/h to 120 km/h in increments of 1.08 km/h. The velocity increment of 1.08 km/h (= 0.3 m/s) is the result of discretizing an initial velocity range between 0 and 30 m/s into 100 equal intervals to create a sufficiently continuous contour plot. Subsequently, changes in DAF will be calculated by subtracting the healthy DAF-velocity plot from the plot corresponding to different points in time or damage scenarios.

4.1. DAF-velocity pattern for healthy state

Figure 7 shows 3D plots of DAF against velocity (km/h) of the vehicle crossing the bridge. Figures 7(a), (b) and (c) illustrate DAFs for all sensors across ¼, ½ and ¾ span respectively.

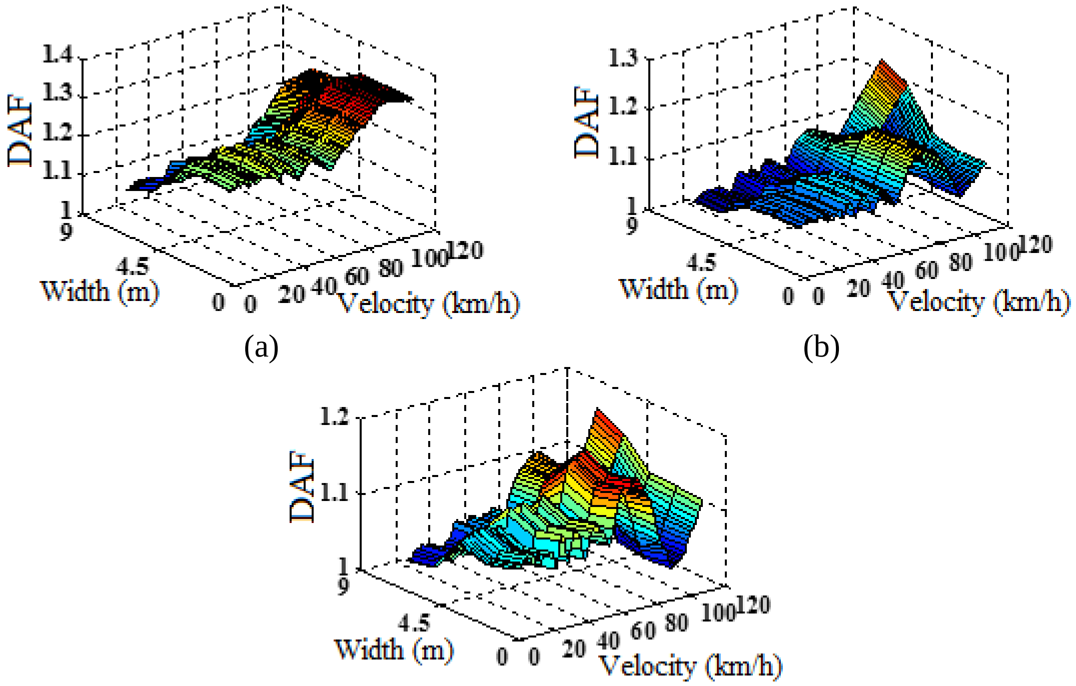

(a) (b)

(c)

Figure 7. DAF at 3 bridge longitudinal locations versus velocity of vehicle crossing healthy bridge: (a) A sensors (1/4 span), (b) B sensors (1/2 span), and (c) C sensors (3/4 span).

From a static point of view, the influence lines of longitudinal bending moment at locations A and C are symmetric with respect to the bridge midspan, and they reach a maximum value when the moving load is positioned on the location under investigation. However, the total static response at A differs from C due to the relative position of the axles on the bridge. For example, most of the truck weight is concentrated in the rear tridem, but when the rear tridem reaches the locations C, the first and second axles will have left the bridge and will not contribute to the bending at that location. Similarly, the dynamic component of the responses at A and C is affected by the relative position of the axles on the bridge and their interaction with the modes of vibration. Figure 7 reveals that DAF at A tends to be higher than DAF at C.

4.2. DAF-velocity pattern for hypothetical damaged state

Figure 8 shows 3D plots of DAF at each of the sensor locations against velocity (km/h) for the case of a 30% stiffness loss modelled as full-through damage (Figure 3(a)).

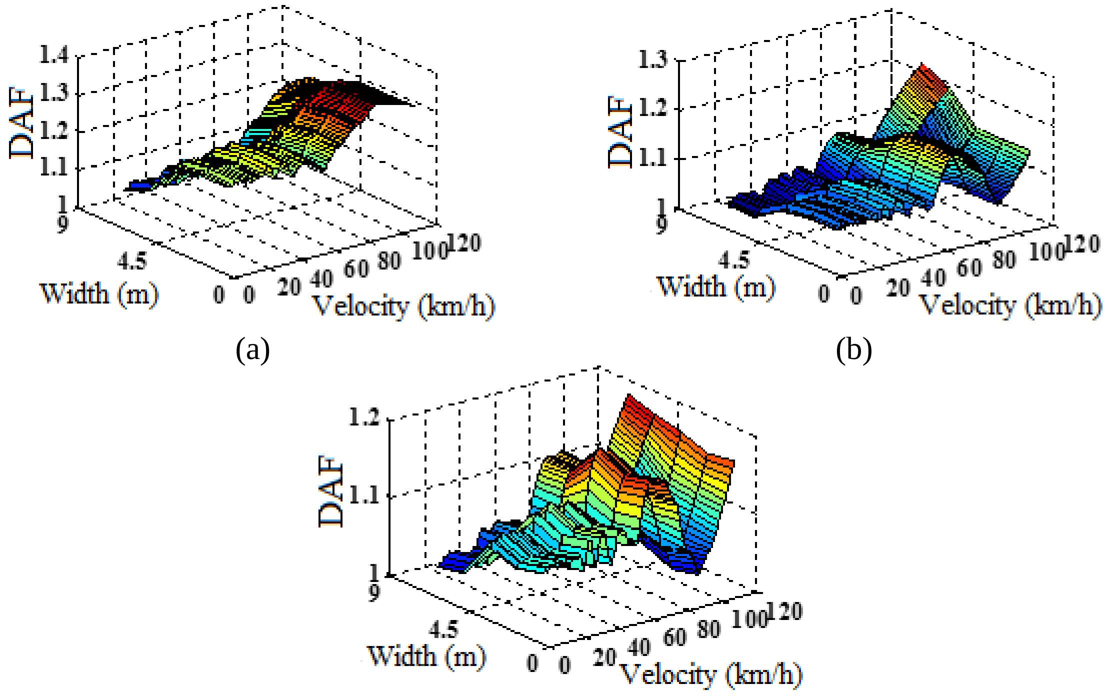

(a) (b)

(c)

Figure 8. DAF at 3 bridge longitudinal locations versus velocity of vehicle crossing a bridge with full-through damage of 30% stiffness loss: (a) A sensors (1/4 span), (b) B sensors (1/2 span), and (c) C sensors (3/4 span).

DAF varies not only longitudinally, but also transversely as illustrated in Figure 9 for C sensors (3/4 span) and velocities of 54 km/h and 55.08 km/h for healthy and damaged conditions. There appears to be an overall increment in DAF when comparing Figure 9(b) in damaged condition with Figure 9(a) in a healthy condition, based on the same sensors and velocities.

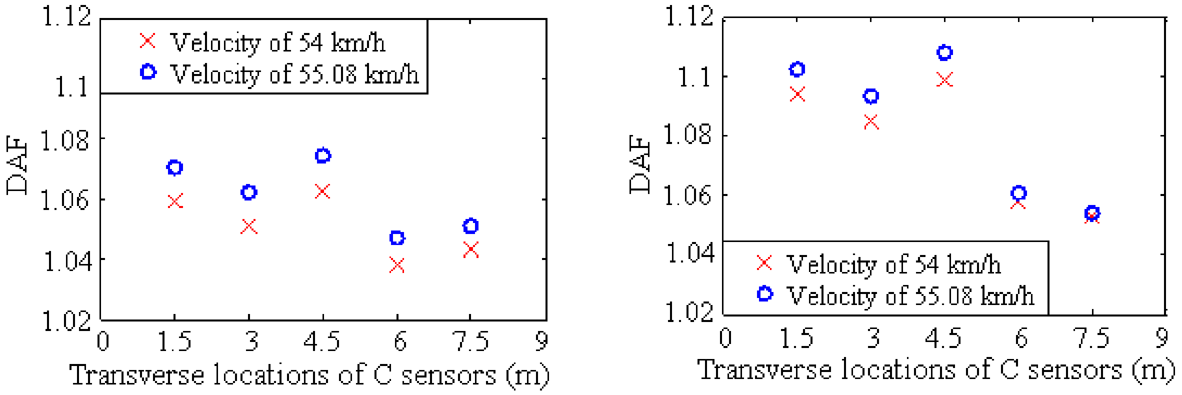

(a) (b)

Figure 9. DAF at C sensors (3/4 span) due to the passage of the vehicle at 54 and 55.08 km/h: (a) healthy condition and (b) full-through damage of 30% stiffness loss.

4.3. Changes in DAF patterns for two points in time

The DAF for a healthy bridge is subtracted from the DAF for a damaged bridge for each velocity and sensor location. I.e., for the case under investigation and C sensors, Figure 9(a) would be subtracted from Figure 9(b) for each of the two velocities: 54 km/h and 55.08 km/h. By repeating this process for every velocity and sensor, it is possible to obtain Figure 10, which shows the change in DAF ("damaged – healthy") for the cases of bridges with full-through damage and stiffness losses of 10% and 30%. As expected, variations in DAF for 10% stiffness loss are not as evident as for 30% stiffness loss.

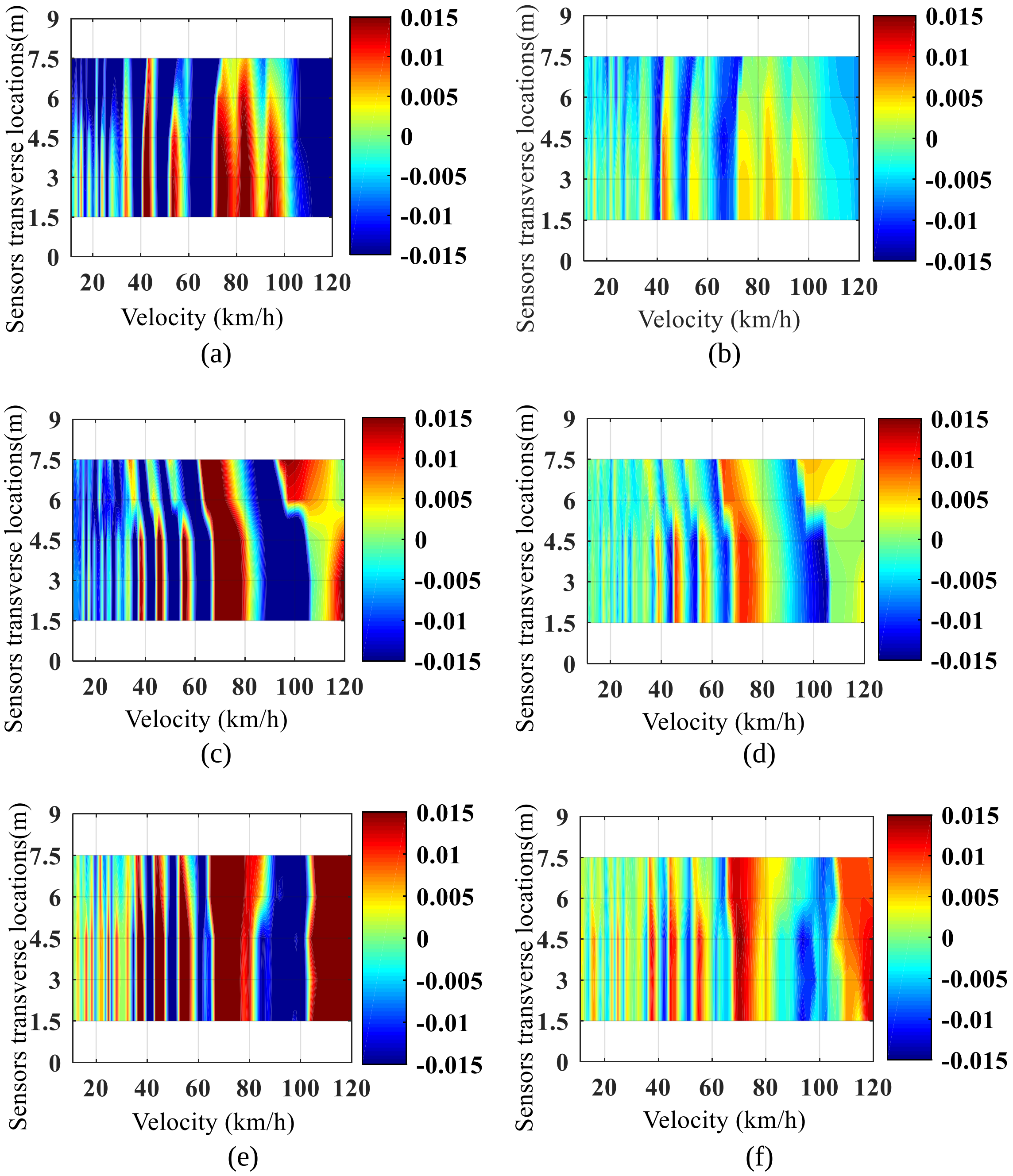

(a) (b) (c) (d) (e) (f)

Figure 10. Changes in DAF due to vehicle on smooth road profile: (a) A sensors (1/4 span) 30% stiffness loss, (b) A sensors (1/4 span) 10% stiffness loss, (c) B sensors (1/2 span) 30% stiffness loss, (d) B sensors (1/2 span) 10% stiffness loss, (e) C sensors (3/4 span), 30% stiffness loss, and (f) C sensors (3/4 span), 10% stiffness loss.

Therefore, positive and negative increments in DAF can develop across a range of velocities when introducing damage. In order to quantify these changes, Equation (10) defines a unique non-dimensional DAF-based Damage Index (DI). The index is obtained by: firstly adding the relative differences in the DAF-velocity pattern of the damaged and healthy bridges for each of the sensor locations with respect to the increment/decrement of the static response in the healthy state (i.e., the denominator given by “DAF – 1”), secondly, dividing the total of relative differences by the number of available sensors and velocities, and finally, multiplying it by 100 to express the relative change in percentage.

$$DI = \left[\frac{1}{n}\sum_{i=1}^{i=n}\left(\frac{1}{m}\sum_{j=1}^{j=m}\left\{\left|\frac{DAF_{ij,2}-DAF_{ij,1}}{DAF_{ij,1}-1}\right|\right\}\right)\right] \times 100 \qquad (10)$$

where $DAF_{ij,1}$ is the DAF at sensor location *i* for velocity *j* for a reference state of the bridge assumed to be healthy and $DAF_{ij,2}$ is the DAF at sensor location *i* for velocity *j* at another state in time to be assessed. The total number of sensor locations is denoted by *n* and the total number of different velocities for each sensor is *m*.

4.4. Influence of sensor locations, damage model and road roughness on DAF-based damage indicator

Table 3 provides DAF-based DI for the six damage scenarios at each of the longitudinal sensor locations (¼, ½ and ¾ span). The results show that C sensors at the ¾ span section are the most sensitive to the full-through damage, part-through damage 1 and part-through damage 2 scenarios.

Table 3. DAF-based damage indicator (%) for the six damage scenarios

Sensors Locations	Stiffness loss percentage	Full-through damage	Part-through damage 1	Part-through damage 2
A	30 %	7.99	5.13	4.28
B		18.34	9.30	10.05
C		26.69	12.64	13.11
A	10 %	2.44	1.62	1.37
B		5.92	3.10	3.22
C		8.47	4.18	4.14

It must be highlighted that the relative changes in percentage are considerably more sensitive to damage than the change in frequencies provided by Table 2. For instance, in the case of a 30% stiffness loss, DI changes by 26.69% (full-through), 12.64% (part-through 1) and 13.11% (part-through 2) compared with frequency changes of –5.23%, –2.35% and –2.35% respectively for the three damaged regions under consideration. In the case of a 10% stiffness loss, DI changes by 8.47% (full-through), 4.18% (part-through 1) and 4.14% (part-through 2) compared with –1.41%, –0.70% and –0.70% respectively. It is also worth to note that unlike other damage detection techniques, the proposed DI does not require sensors relatively close to the damaged portion of the bridge to be effective. In fact, C sensors are farther apart from the damaged region than A or B sensors. The sensors A at ¼ span are the least sensitive to the damaged scenario presented in Figure 3. As a result of damage, the dynamic component of the response in locations A and C will vary slightly in frequency and in amplitude, but given that, overall, the values of DAF at locations C are lower than at locations A (Figure 7), the relative dynamic increments in DAF used to identify damage will be felt more strongly at C than at A. For the same reason, relative dynamic increments in DAF at B are more sensitive to damage than relative dynamic increments at A, although they are outperformed by sensors at C. It must be noted that these conclusions correspond to a situation with a smooth profile and that they must be interpreted with caution before being generalized to other scenarios where the location of the road irregularities will govern the DAF pattern.

Healthy and damaged bridges are now assumed to be paved with very good and good road classes [34]. Contour plots for the resulting DAFs are obtained when subtracting the DAF of the healthy bridge from the bridges affected by full-through damage of 30% and 10% stiffness. The latter are shown in Figures 11 and 12 for very good and good road classes respectively. For a given section (¼, ½ or ¾ span), the changes in DAF appears to show a similar pattern for the 30% stiffness loss regardless of the road class. The same can be said about the patterns of changes in DAF for 10% stiffness loss. Obviously, lighter colours (smaller changes in DAF values = less damage) are visible for the 10% stiffness loss than for the 30%.

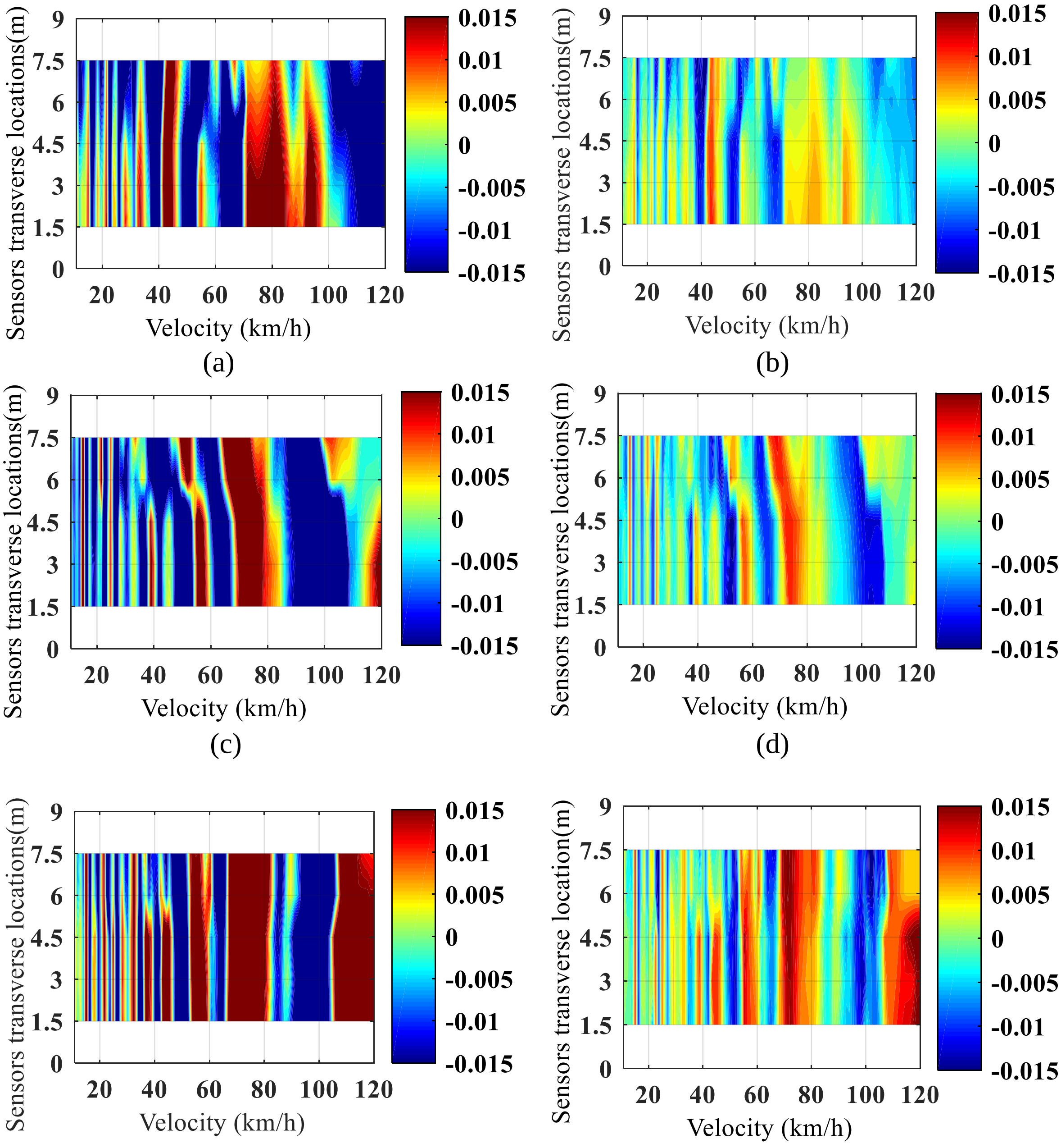

(a) (b) (c) (d) (e) (f)

Figure 11. Changes in DAF on a class 'A' road profile: (a) A sensors (1/4 span), 30% stiffness loss, (b) A sensors (1/4 span), 10% stiffness loss, (c) B sensors (1/2 span), 30% stiffness loss, (d) B sensors (1/2 span), 10% stiffness loss, (e) C sensors (3/4 span), 30% stiffness loss, and (f) C sensors (3/4 span), 10% stiffness loss.

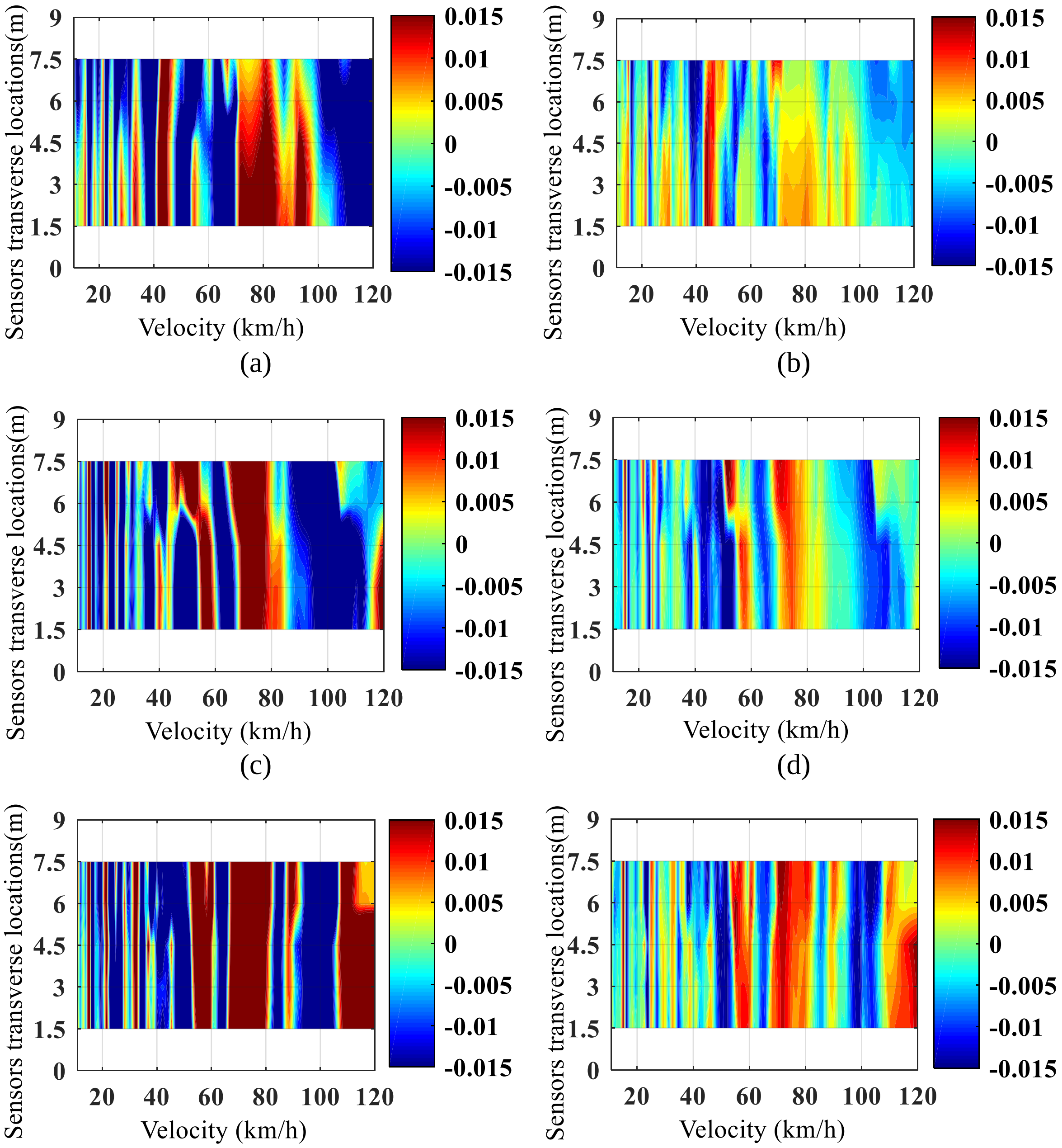

(a) (b)

(c) (d)

(e) (f)

Figure 12. Changes in DAF on a class ‘B’ road profile: (a) A sensors (1/4 span), 30% stiffness loss, (b) A sensors (1/4 span), 10% stiffness loss, (c) B sensors (1/2 span), 30% stiffness loss, (d) B sensors (1/2 span), 10% stiffness loss, (e) C sensors (3/4 span), 30% stiffness loss, and (f) C sensors (3/4 span), 10% stiffness loss.

Table 4 allows assessing the influence of road roughness on the DAF-based DI. In the table, DIs are calculated for a combination of 3 damage locations with 2 degrees of damage severity, 3 longitudinal locations for the sensors and 2 road profiles. Table 4 illustrates that the highest DI is detected by C sensors at ¾ bridge span paved with a good road class and sustained full-through damage of 30 % stiffness loss.

Table 4. DAF-based damage indicator (%) for the 12 scenarios varying road roughness

Road profile type	Stiffness loss percentage	Sensors Locations	Full-through damage	Part-through damage 1	Part-through damage 2
‘very good’	30 %	A	6.85	4.76	4.00
		B	17.51	9.38	9.87
		C	23.95	12.57	12.38
	10 %	A	2.25	1.53	1.29
		B	6.18	3.20	3.22
		C	8.15	3.98	3.89
‘good’	30 %	A	6.58	4.71	3.72
		B	23.43	15.96	20.24
		C	29.09	14.48	14.10
	10 %	A	2.12	1.49	1.19
		B	11.70	4.19	4.07
		C	9.46	4.43	4.27

Similar to Table 3 (smooth profile), sensors A at ¼ span showed to be the least sensitive to the damaged scenarios also in Table 4 (rough profile), although they are still about twice more sensitive than the frequency change given by Table 2. For all longitudinal sensor locations, DIs increase from part-through to full-through and from 10% stiffness loss to 30% stiffness loss, from a minimum 1.19% (10% part-through 2 stiffness loss in a good profile) to a maximum 6.85% (30% full-through stiffness loss in a very good profile) for sensors A, from a minimum 3.20% (10% part-through 1 stiffness loss in a very good profile) to a maximum 23.43% (30% full-through stiffness loss in a good profile) for sensors B, and from a minimum 3.89% (10% part-through 2 stiffness loss in a very good profile) to a maximum 29.09% (30% full-through stiffness loss in a good profile) for sensors C. Overall, for a given damage extent (part- and full-through) and severity (10% or 30%), DIs are more consistent the smoother the profile. For example, adopting sensors A, DI goes from 2.44% to 7.99% (difference of 5.55%) when increasing full-through damage from 10% to 30% stiffness loss in the case of a smooth profile (Table 3). However, DI for sensors A go from 2.25% to 6.85% (difference of 4.60%) in the case of a very good rough profile and from 2.12% to 6.58% (difference of 4.46%) in the case of a good rough profile (Table 4). Similar conclusions are obtained with other locations of sensors and damage. It has been seen how the amplitude of the DAF-velocity pattern has an impact on the sensitivity of the three measurement locations under investigation. C sensors clearly outperform B and A sensors for all damage scenarios with a smooth road surface and with a very good road surface. However, when increasing road roughness to a good condition, there are damage scenarios where B sensors lead to higher DI values than C sensors. Rougher profiles will have a more prominent influence on the DAF-velocity pattern, and the presence of significant road irregularities at critical locations will induce relatively higher values of DAF at some sensor locations than others. Therefore, the ideal sensor location that will maximize DI will depend not only on the bridge, specific vehicle and damage scenario but also on the road roughness and on the spatial distribution of the road irregularities (i.e., road phases and bumps).

4.5. Influence of noise on DAF-based damage indicator

Figures 13 (DAF versus vehicle velocity at C sensors) carry out the same analysis as in Figures 7(c) and 8(c), except that this time, 20% noise has been added to the calculated DAF (i.e., to simulate an error derived from parameters necessary for the algorithm such as velocity or configuration of the vehicle).

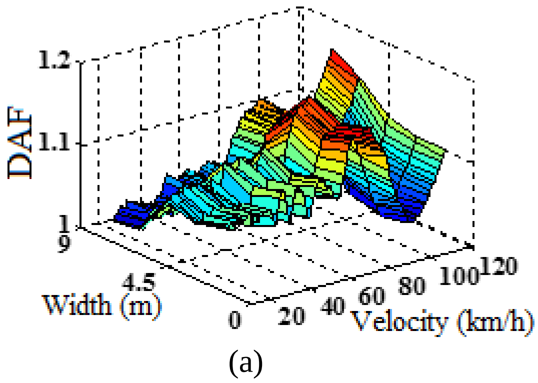

Figure 13. DAF versus vehicle velocity at C sensors (3/4 span) with a 20% noise: (a) healthy bridge and (b) bridge with full-through damage of 30% stiffness loss.

The noise component has been randomly generated based on values from a normal distribution with zero mean and unit standard deviation multiplied by the noise level (i.e., 20% and 10%) and standard deviation of the noise-calculated DAF [47]. The shapes of the corrupted surfaces in Figures 13 are similar to those seen in Figures 7(c) and 8(c) (for DAF containing no noise). However, the addition of noise has the effect of producing surfaces that are less smooth than in the noise-free case, i.e., there is less consistency between the calculated DI of DAF (Sec. 4.3) at adjacent sensors. The source of this inconsistency can be understood by examining Figures 14(a) and (b) representing sections at a velocity of 58.32 km/h for both noise-free-DAFs and those containing 10% and 20% noise at sensor locations C for a healthy bridge and a bridge with 30% stiffness loss.

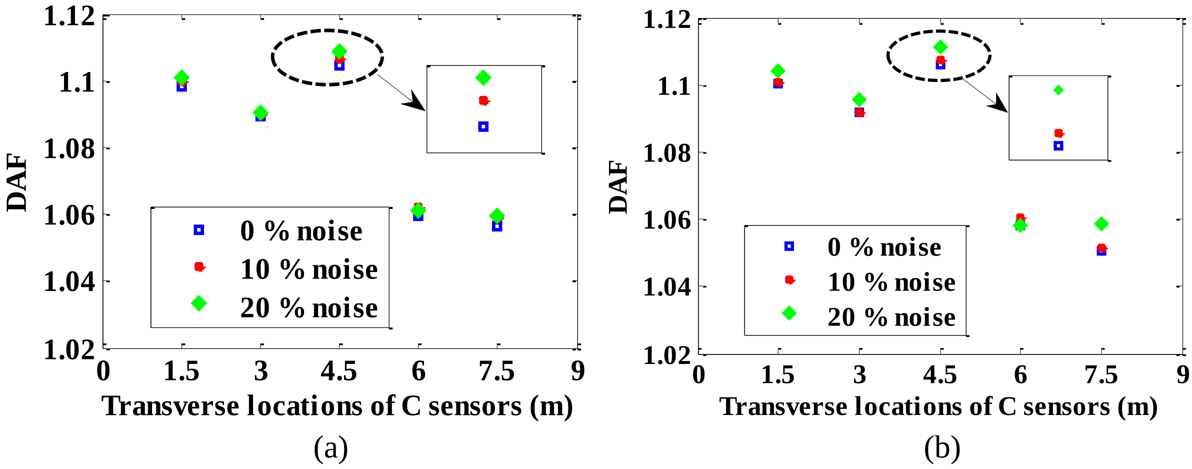

Figure 14. DAF at C sensors (3/4 span) with 0%, 10% and 20% noise for a velocity of 58.32 km/h: (a) healthy bridge and (b) bridge with full-through damage of 30% stiffness loss.

Moreover, DAF-based DI are re-calculated allowing for added noise. Tables 5 and 6 provide DIs of DAF corrupted by 10% and 20% noise respectively, for each of the longitudinal sensor locations (¼, ½ and ¾ span). In comparison to Table 3, the added noise only has a slight impact on the Dis for the full-through or part-through damage scenarios under investigation. Using again the least sensitive of all sensors as reference, DI for sensors A, it goes from 2.56% (10% full-through stiffness loss) to 7.87% (30% full-through stiffness loss), i.e., a difference of

5.31% in the case of 10% noise (Table 5), and from 3.19% (10% full-through stiffness loss) to 7.76% (30% full-through stiffness loss) , i.e., a difference of 4.57% in the case of 20% noise (Table 6), compared with going from 2.44% to 7.99% (difference of 5.55%) in the absence of noise (Table 3).

Table 5. DAF-based damage indicator (%) for the six damage scenarios influenced by 10% noise

Sensors Locations	Stiffness loss percentage	Full-through damage	Part-through damage 1	Part-through damage 2
A	30 %	7.87	5.12	4.36
B		17.88	9.08	10.05
C		26.24	12.29	12.94
A	10 %	2.56	1.81	1.68
B		6.10	3.48	3.68
C		8.49	4.64	4.36

Table 6. DAF-based damage indicator (%) for the six damage scenarios influenced by 20% noise

Sensors Locations	Stiffness loss percentage	Full-through damage	Part-through damage 1	Part-through damage 2
A	30 %	7.76	5.23	4.59
B		17.76	9.58	9.96
C		25.88	12.63	13.16
A	10 %	3.19	2.53	2.24
B		6.48	4.25	4.48
C		8.64	5.48	5.19

4.6. Influence of velocity on DAF-based damage indicator

Table 7 provides DAF-based DIs considering a smooth profile and a number of velocity ranges: 49.68 to 60.48 km/h, 61.56 to 72.36 km/h, 73.44 to 84.24 km/h, 85.32 to 96.12 km/h and 97.20 to 108 km/h. The results show that the longitudinal sensor locations (¼, ½ and ¾ span) are most sensitive to the damages under investigation at the velocity range of 61.56 to 72.36 km/h.

The optimal velocity range may, however, vary for other VBI and damage specifications, depending on the numerous parameters affecting the response. For this reason, the DAF-based DI would ideally be calculated for a wide range of velocities enabling to maximize the sensitivity to damage regardless of the parameters defining the VBI scenario. Figures 15(a) and (b) illustrates the variation of DI with velocity range for the case of full-through damage with 30% and 10% stiffness loss respectively. In this figure, sensors C experience the largest increments in DI regardless of the stiffness loss and the velocity range.

Table 7. DAF-based damage indicator (%) for the six damage scenarios and different velocity ranges

Sensors Locations	velocity range (km/h)	Stiffness loss percentage	Full-through damage	Part-through damage 1	Part-through damage 2
A	49.68 - 60.48	30 %	9.42	6.45	5.62
B			22.77	10.78	11.76
C			23.96	11.32	12.14
A	61.56 - 72.36	30 %	15.38	6.85	8.30
B			32.70	18.97	14.46
C			41.59	21.34	17.59
A	73.44 - 84.24	30 %	6.00	4.95	4.44
B			9.62	7.09	4.04
C			12.60	8.29	5.83
A	85.32 - 96.12	30 %	2.90	3.61	2.45
B			17.48	6.74	8.11
C			18.20	5.98	8.75
A	97.20 - 108	30 %	2.73	2.77	1.49
B			24.23	11.43	15.11
C			41.36	15.70	18.83
A	49.68 - 60.48	10 %	3.20	2.11	1.89
B			7.09	3.49	3.70
C			7.26	3.40	3.59
A	61.56 - 72.36	10 %	4.78	2.11	2.63
B			11.06	6.22	4.71
C			12.80	6.59	5.33
A	73.44 - 84.24	10 %	1.75	1.60	1.48
B			3.73	2.47	1.46
C			4.76	2.87	2.01
A	85.32 - 96.12	10 %	1.03	1.13	0.80
B			4.43	2.07	2.28
C			4.62	1.74	2.56
A	97.20 - 108	10 %	0.76	0.88	0.47
B			8.54	3.83	5.42
C			11.11	5.47	5.74

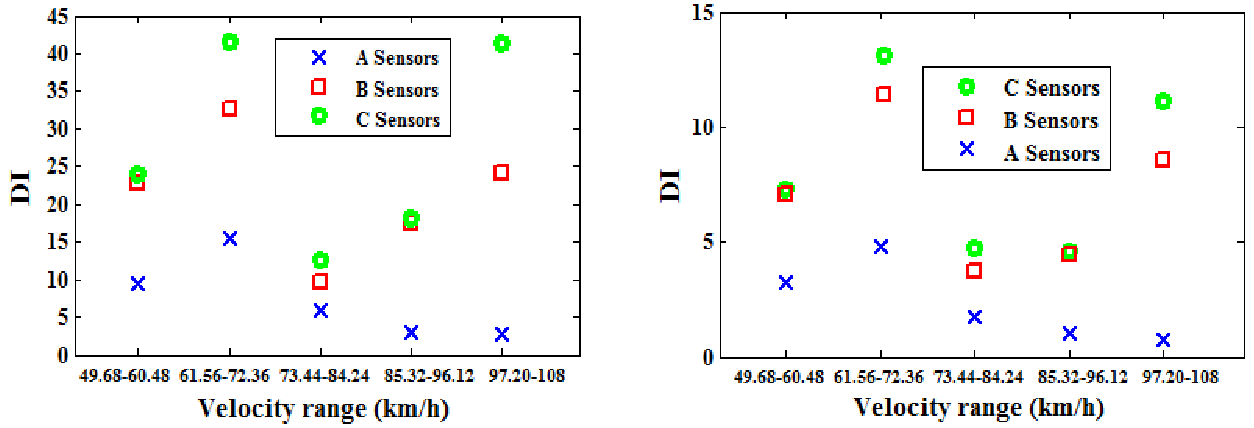

(a) (b)

Figure 15. DAF-based DI for full through-damage and different velocity ranges: (a) 30% stiffness loss and (b) 10% stiffness loss.

5. Conclusions

This paper has put forward a new level I damage detection method based on the pattern of bridge DAF versus vehicle velocity. In order to apply this method, the vehicle velocity, the number of axles and their spacing and weights need to be established on-site by means of a WIM or B-WIM system. B-WIM systems commonly measure strains at the bottom of a bridge deck to estimate the static weights of the axles crossing the bridge. The damage detection method proposed in this paper also uses strains as input, and thus, it has the potential for extending the capabilities of B-WIM systems, typically limited to the collection of data about traffic loads. The method has been tested with the simulated response of a simply supported FE plate of 20 m × 9 m subjected to a 3-D 5-axle articulated vehicle model. DAF has been obtained at three equally spaced longitudinal locations (¼, ½ and ¾ span) which enable to gather a broad picture of DAF patterns along the bridge length. A unique non-dimensional DAF-based DI has been proposed based on calculating the relative differences in the DAF-velocity pattern of two bridge conditions with respect to the original dynamic increment for every sensor location. The DI yields higher DAF damage indices for larger damaged areas and for more severe levels of damage. The DI has also been shown to be hardly sensitive to the road roughness and noise investigated. Generally speaking, for the same location and level of damage, most of the damage indices are slightly higher for a smooth profile than for very good class profile, and damage indices on a very good class profile are higher than on a good class profile. For a given road class, further work is needed to address how the randomness of the road carpet will affect the performance of the method, i.e., randomly varying the phase of the power spectral density. Although one longitudinal sensor location may have been enough to detect damage, the use of multiple longitudinal locations adds robustness for dealing with more difficult cases (i.e., rough profile and low level of damage located far from the sensors). When adding noise levels of 10% or 20% to DAF measurements, the damage has continued to be accurately identified. Although damage has been noticeable across a wide range of velocities, it is possible to identify optimal velocities more sensitive to a particular damage. If a WIM system was available on site, the new method has proven to be a promising alternative to other level I damage detection techniques unable to distinguish small changes in natural frequencies due to damage or strongly dependent on having sensors installed relatively close to the damage.

Acknowledgements

The authors wish to express their gratitude for the financial support received from Al-Anbar University and the Iraqi ministry of higher education towards this research.

6. References

[1] F. S. Wong and J. T. P. Yao, "Health monitoring and structural reliability as a value chain," *Comput. Civ. Infrastruct. Eng.*, vol. 16, no. 1, pp. 71-78, Jan. **2001**.

[2] A. A. Mufti, B. Bakht, G. Tadros, A. T. Horosko, and G. Sparks, *Sensing issues in civil structural health monitoring*. Dordrecht: Springer Netherlands, **2005**.

[3] M. Döhler, F. Hille, L. Mevel and W. Rücker, "Structural health monitoring with statistical methods during progressive damage test of S101 Bridge," *Eng. Struct.*, vol. 69, pp.183-193, **2014**.

[4] H. Liu, X. Wang and Y. Jiao, "Effect of temperature variation on modal frequency of reinforced concrete slab and beam in cold regions," *Shock and Vibration*, vol. 2016, article id. 4792786, **2016**.

[5] M. D. Spiridonakos, E. N. Chatzi and B. Sudret, "Polynomial chaos expansion models for the monitoring of structures under operational variability," *ASCE-ASME Journal of Risk and Uncertainty in Engineering Systems, Part A: Civil Engineering*, vol. 2, no. 3,

Sep. **2016**.

[6] A. Deraemaeker, E. Reynders, G. De Roeck, and J. Kullaa. “Vibration-based structural health monitoring using output-only measurements under changing environment,” *Mechanical Systems and Signal Processing*, vol. 22, pp. 34-56, **2008**.

[7] A.-M. Yan, G. Kerschen, P. De Boe and J.-C. Golinval, “Structural damage diagnosis under varying environmental conditions-Part I: A linear analysis,” *Mechanical Systems and Signal Processing*, vol. 19, no. 4, pp. 847-864, **2005**.

[8] Y. Shokrani, V. K. Dertimanis, E. N. Chatzi and M. Savoia, "Structural damage localization under varying environmental conditions", 11th HSTAM International Congress on Mechanics, Athens, Greece, 27 - 30 May **2016**.

[9] E. Reynders, G. Wursten and G. De Roeck, "Output-only structural health monitoring in changing environmental conditions by means of nonlinear system identification," Structural Health Monitoring, vol. 13, no. 1, pp. 82-93, **2013**.

[10] A. Rytter, Vibrational based inspection of civil engineering structures. fracture and dynamics, no. 44, vol. R9314, Dept. of Building Technology and Structural Engineering, Aalborg University, Aalborg, **1993**.

[11] W. Fan and P. Qiao, “Vibration-based damage identification methods: A review and comparative study,” *Struct. Heal. Monit.*, vol. 10, no. 1, pp. 83-111, Jan. **2011**.

[12] M.P. Limongelli, E. Chatzi, M. Döhler, G. Lombaert and E. Reynders, “Towards extraction of vibration-based damage indicators,” 8th European Workshop on Structural Health Monitoring (EWSHM 2016), Bilbao, Spain, 5-8 Jul. **2016**.

[13] D. Cebon, *Handbook of vehicle-road interaction*. Swets & Zeitlinger Lisse, The Netherlands, **1999**.

[14] D. Cantero and A. González, “Bridge damage detection using weigh-in-motion technology,” *J. Bridg. Eng.*, no. 1, pp. 1-10, **2014**.

[15] S. Brady, E. O’Brien, and A. Žnidarič, “Effect of vehicle velocity on the dynamic amplification of a vehicle crossing a simply supported bridge,” *J. Bridg. Eng.*, vol. 11, no. 2, pp. 241-249, **2006**.

[16] Y. Li, E. OBrien, and A. González, “The development of a dynamic amplification estimator for bridges with good road profiles,” *J. Sound Vib.*, vol. 293, no. 1–2, pp. 125-137, May **2005**.

[17] O. Mohammed, and A. González, “Static and dynamic moments for any plane within a straight solid slab bridge caused by the crossing of a truck,” *Eng. Struct.*, vol. 150, pp. 465-480, **2017**.

[18] F. R. Rofooei, A. Enshaeian, and A. Nikkhoo, “Dynamic response of geometrically nonlinear, elastic rectangular plates under a moving mass loading by inclusion of all inertial components,” *J. Sound Vib.*, vol. 394, pp. 4975-14, **2017**.

[19] L. Deng, Y. Yu, Q. Zou, and C. S. Cai, “State-of-the-Art review of dynamic impact factors of highway bridges,” *J. Bridg. Eng.*, vol. 20, no. 5, pp. 4014080-1-14, May **2014**.

[20] A. González, E. J. OBrien, D. Cantero, Y. Li, J. Dowling, and A. Žnidarič, “Critical speed for the dynamics of truck events on bridges with a smooth road surface,” *J. Sound Vib.*, vol. 329, no. 11, pp. 2127-2146, May **2010**.

[21] D. Cantero, A. González, and E. J. OBrien, “Comparison of bridge dynamic amplifications due to articulated 5-axle trucks and large cranes,” *Balt. J. Road Bridg. Eng.*, vol. 6, no. 1, pp. 39-47, Mar. **2011**.

[22] W. Zhang and C. S. Cai, “Reliability-based dynamic amplification factor on stress ranges for fatigue design of existing bridges,” *J. Bridg. Eng.*, vol. 18, no. 6, pp. 538-552, Jun. **2013**.

[23] A. González, D. Cantero, and E. J. OBrien, “Dynamic increment for shear force due to heavy vehicles crossing a highway bridge,” *Comput. Struct.*, vol. 89, no. 23-24, pp. 2261-

2272, Dec. **2011**.

[24] H. Aied, and A. González, "Theoretical response of a simply supported beam with a strain rate dependant modulus to a moving load," *Eng. Struct.*, vol. 77, no. 15, pp. 95-105, **2014**.

[25] O. Mohammed and A. González, "Footprint caused by a vehicle configuration on the dynamic amplification of the bridge response," *J. Phys. Conf. Ser.*, vol. 628, no. 1, p. 12064, Jul. **2015**.

[26] C. W. Kim, M. Kawatani, and K. B. Kim, "Three-dimensional dynamic analysis for bridge-vehicle interaction with roadway roughness," *Comput. Struct.*, vol. 83, no. 19-20, pp. 1627-1645, Jul. **2005**.

[27] D. Cantero, T. Arvidsson, E. OBrien, and R. Karoumi, "Train–track–bridge modelling and review of parameters," *Struct. Infrastruct. Eng.*, vol. 12, no. 9, pp. 1051-1064, **2015**.

[28] A. González, "Vehicle-bridge dynamic interaction using finite element modelling," *Lipovic, I.(ed.). Finite Elem. Anal.*, pp. 637-662, **2010**.

[29] C. Broquet, S. F. Bailey, M. Fafard, and E. Brühwiler, "Dynamic behavior of deck slabs of concrete road bridges," *J. Bridg. Eng.*, vol. 9, no. 4, pp. 137-146, Mar. **2004**.

[30] L. Deng and C. S. S. Cai, "Development of dynamic impact factor for performance evaluation of existing multi-girder concrete bridges," *Eng. Struct.*, vol. 32, no. 1, pp. 21-31, Jan. **2010**.

[31] D. Huang, T. Wang, and M. Shahawy, "Impact analysis of continuous multigirder bridges due to moving vehicles," *J. Struct. Eng.*, vol. 118, no. 12, pp. 3427-3443, Dec. **1992**.

[32] D. Z. Huang, T. Lo Wang, and M. Shahawy, "Dynamic behavior of horizontally curved I-girder bridges," *Comput. Struct.*, vol. 57, no. 4, pp. 703-714, Nov. 1995.

[33] C. W. Kim, M. Kawatani, and Y. R. Kwon, "Impact coefficient of reinforced concrete slab on a steel girder bridge," *Eng. Struct.*, vol. 29, no. 4, pp. 576-590, **2007**.

[34] International Organization for Standardization (ISO), "Mechanical vibration - Road surface profiles - Reporting of measure data, ISO8608 (BS7853:1996)," **1995**.

[35] D. Cebon and D. E. Newland, "Artificial generation of road surface topography by the inverse F.F.T. Method," *Veh. Syst. Dyn.*, vol. 12, no. 1-3, pp. 160-165, Jul. **1983**.

[36] N. K. Harris, E. J. OBrien, and A. González, "Reduction of bridge dynamic amplification through adjustment of vehicle suspension damping," *J. Sound Vib.*, vol. 302, no. 3, pp. 471-485, May **2007**.

[37] M. W. Sayers and S. M. Karamihas, "Interpretation of Road roughness profile data—final report," **1996**.

[38] MATLAB. Version r 2014 a, The MathWorks, https://aj-hub.ucd.ie/, **2014**.

[39] D. Cantero, E. J. O'Brien, and A. González, "Modelling the vehicle in vehicle–infrastructure dynamic interaction studies," *Proc. Inst. Mech. Eng. Part K J. Multi-body Dyn.*, vol. 224, no. 2, pp. 243-248, Jan. **2009**.

[40] M. Green and D. Cebon, "Dynamic interaction between heavy vehicles and highway bridges," *Comput. Struct.*, vol. 62, no. 2, pp. 253-264, **1997**.

[41] A. González, C. Rowley, and E. J. OBrien, "A general solution to the identification of moving vehicle forces on a bridge," *Int. J. Numer. Methods Eng.*, vol. 75, no. 3, pp. 335-354, Jul. **2008**.

[42] J. N. Reddy, *Energy Principles and variational methods in applied mechanics*. John Wiley & Sons, **2002**.

[43] E. O. Brien, D. L. Keogh, and A.O. Connor, *Bridge Deck Analysis*. CRC Press, **2015**.

[44] Y. C. Li, "Factors affecting the dynamic interaction of bridges and vehicle loads," PhD thesis, Civil Engineering School, University College Dublin, Ireland, **2006**.

[45] J. K. Sinha, M. I. Friswell, and S. Edwards, "Simplified models for the location of cracks in beam structures using measured vibration data," *J. Sound Vib.*, vol. 251, no. 1, pp. 13-

38, Mar. **2002**.

[46] A. González, J. Dowling, E. J. O'Brien, and A. Žnidarič, "Testing of a bridge weigh-in-motion algorithm utilising multiple longitudinal sensor locations," *J. Test. Eval.*, vol. 40, no. 6, p. 104576, Nov. **2012**.

[47] X. Q. Zhu and S. S. Law, "Wavelet-based crack identification of bridge beam from operational deflection time history," *Int. J. Solids Struct.*, vol. 43, no. 7-8, pp. 2299-2317, **2006**.